SUPPORTING INFORMATION

for

Boosted reverse water-gas shift activity *via* exsolved Cu and Ni in silicalite-1

Jedy Prameswari,[a] Pei-Tung Chou,[a] Ming-Yuan Hung,[b] Po-Yang Peng,[c] Ying-Rui Lu,[c] Chi-Liang Chen,[c] Hong-Kang Tian, *[a,b,d] and Yu-Chuan Lin [*a]

[a]Department of Chemical Engineering, National Cheng Kung University, Tainan 70101, Taiwan.

Email: hktian@gs.ncku.edu.tw; yclin768@mail.ncku.edu.tw

[b]Program on Smart and Sustainable Manufacturing, Academy of Innovative Semiconductor and Sustainable Manufacturing, National Cheng Kung University, Tainan 70101, Taiwan

[c]National Synchrotron Radiation Research Center, Hsinchu 30076, Taiwan.

[d]Hierarchical Green-Energy Materials (Hi-GEM) Research Center, National Cheng Kung University, Tainan 70101, Taiwan

Experimental section

Materials: Nickel (II) nitrate hexahydrate (98%, SHOWA), copper (II) nitrate trihydrate (99%, SHOWA), colloidal silica (LUDOX HS-30, Sigma-Aldrich), tetrapropylammonium hydroxide (TPAOH, 40%, Alfa Aesar), ethylene diamine (EN, 99%, Acros Organics), and sodium hydroxide (NaOH, 97%, SHOWA) were used without further purification. Colloidal silica was used as the silica source of silicalite-1 (S-1).

M@S-1 catalyst preparation: The metal-embedded S-1 (Me@S-1; Me = Cu or Ni) were synthesized using a modified ligand-protecting in-situ method.[1] The 2 *%w/w* metal solution was prepared by dissolving the metal precursor (Ni or Cu) in 55 mL of deionized water and 0.5 g of ethylene diamine, followed by stirring at 300 rpm for 30 minutes. Subsequently, 0.5 g of NaOH and 1.376 g of TPAOH were introduced and stirred for an additional 30 minutes. The solution was then subjected to dropwise addition of 8.3 g of colloidal silica over 8 h under agitation. The resulting mixture was transferred to a Teflon-lined autoclave for a hydrothermal treatment at 180 ^{o}C for 72 h. The remaining paste was collected by filtration and dried at 80 ^{o}C for 12 h and then calcined at 550 ^{o}C for 6 h. The resulted catalysts were sieved in 40-80 mesh size for uniformity and exsolved via the reduction step at 800 ^{o}C for Ni@S-1 and at 500 ^{o}C for Cu@S-1 for 2 h (10 ^{o}C/min) under 20% H_2/N_2 stream in a fixed bed reactor system. The exsolved catalyst was affiliated with a "-red"; e.g., exsolved Me@S-1 was denoted as Me@S-1-red. The exsolved catalysts were passivated under 1% O_2/N_2 for 1 h before subjected to ex-situ characterizations.

Me/S-1 catalyst preparation: The Me/S-1 catalysts were synthesized using the incipient wetness impregnation method. A 2 *%w/w* metal solution (Ni or Cu) was prepared by dissolving the metal in an appropriate amount of deionized water and then impregnating it onto the calcined S-1 support. The mixture was subsequently dried at 80 ^{o}C for 12 h and then calcined at 550 ^{o}C for 6 h. The resulting catalysts were sieved, reduced, and passivated under the same conditions as the Me@S-1 catalyst preparation. The reduced catalyst was denoted as Me/S-1-red.

Catalyst characterization: In-situ X-ray absorption spectroscopy (XAS) at the Ni *K*-edge was analyzed in fluorescence mode at TPS-32A, National Synchrotron Radiation Research Center, Taiwan. The in-situ XAS was conducted under CO_2 and H_2 environments to investigate the behavior of Ni and Cu species in the temperature range of 200-500°C. Data analysis was performed using Athena and Artemis software (version 0.9.26). X-ray photoelectron

spectroscopy (XPS) spectra were recorded with a PHI 5000 VersaProbe spectrometer, equipped with a monochromatized aluminum source (λ = 1486.6 eV). Samples were placed in a transport chamber to prevent air exposure. The crystallinity of the catalysts was assessed using X-ray diffractometry (XRD) with a Rigaku D/Max-IIB instrument, utilizing Cu-Kα as the radiation source. Catalyst composition was determined via Inductively Coupled Plasma Atomic Emission Spectroscopy (ICP-AES, Kontron S-35). Porosity measurements were conducted with an automated N_2 physisorption analyzer (Micrometrics ASAP 2020). High resolution transmission electron microscope (HR-TEM) imaging was conducted using JEOL JEM-2100F Cs STEM electron microscope.

The profile of H_2 temperature-programmed reduction (H_2-TPR) and NH_3 temperature-programmed desorption (NH_3-TPD) were systematically recorded using Autochem II (Micrometrics) equipped with a thermal conductivity detector. Passivated samples underwent in-situ reduction in the Autochem II at 300°C for 1 hour before testing. In-situ infrared Fourier transform spectroscopy (in-situ DRIFTS, Thermo Scientific Nicolet iS50 spectrometer) with a diffuse reflectance cell (Praying Mantis, Harrick Scientific) was performed for CO_2/H_2 switching test and CO-DRIFTS at 50 °C. Pyridine-IR (Py-IR) was analyzed by using an in-situ quartz cell (transmission mode, Dalian Xuanyu Technology).

Activity test: The catalytic performance test was performed in a fixed-bed reactor system. The feed comprised a mixture of $H_2/N_2/CO_2$ (v/v/v = 37.5/50/12.5), and the reaction was performed at 250 °C, 300 °C, 350 °C, and 400 °C maintaining a pressure of 1 atm and gas hourly space velocity (GHSV) of 6000 mL g_{cat} h^{-1}. The reactor system was interconnected with a gas chromatograph (GC, SRI 8610C). Data was collected under steady state conditions in triplicates. CO_2 conversion, CO and CH_4 selectivity, and RWGS conversion (X_{RWGS}) were determined using the following equations:

$$CO_2\ conversion = \frac{n_{CO_2,in} - n_{CO_2,out}}{n_{CO_2,in}} \times 100\%$$

$$CO\ selectivity = \frac{n_{CO}}{n_{CO_2,in} - n_{CO_2,out}} \times 100\%$$

$$CH_4\ selectivity = \frac{n_{CH_4}}{n_{CO_2,in} - n_{CO_2,out}} \times 100\%$$

$$X_{RWGS} = \frac{n_{CO}}{n_{CO_2,in}} \times 100\%$$

where $n_{CO_2,in}$ and $n_{CO_2,out}$ are the moles of the CO_2 feed and the unreacted CO_2, respectively; n_{CO} and n_{CH_4} are the moles of CO and CH_4 products detected at the outlet of the reactor, respectively.

Atomic Structure Construction

The CO adsorption on Ni@S-1-red and Cu@S-1-red was modelled using Ni and Cu metal surfaces as approximations for the reduced Ni and Cu metal clusters in Ni@S-1-red and Cu@S-1-red, respectively. The bulk structures of Ni and Cu were constructed in their stable cubic phase (space group: $Fm\bar{3}m$). After geometry optimization using Density Functional Theory (DFT), the relaxed lattice parameters of Ni and Cu bulk structures closely matched experimental values, with deviations of less than 2%, as shown in Table S4. The (111) surface was selected for further analysis as it is reported in the literature as the most stable surface orientation for both Ni and Cu.[2, 3] To prevent interactions between periodically repeated slabs, a 15 Å vacuum gap was introduced. The optimal number of surface layers was determined by evaluating the total energy per atom for surface structures as the number of layers varied. The convergence of total energy is presented in Figure S19, based on which 11 layers for the Ni slab and 9 layers for the Cu slab were selected for subsequent CO adsorption studies. The calculated surface energies for Ni and Cu (111) surfaces are 1.68 and 1.14 J/m^2, respectively, in agreement with previous studies.[2, 4] For CO adsorption analysis, potential adsorption sites on the Ni and Cu (111) surfaces were identified using Delaunay triangulation as implemented in Pymatgen.[5] This algorithm follows four steps: (1) identify sites within a height threshold along the Miller index of the highest site, (2) generate a network of surface sites using Delaunay triangulation, (3) assign on-top, bridge, and hollow adsorption sites at the nodes, edges, and face centers of the triangulation, and (4) place molecules at these adsorption sites. Although Ni and Cu share the same $Fm\bar{3}m$ space group, their optimized lattice parameters differ slightly, with Ni at 3.52 Å and Cu at 3.63 Å, leading to small variations in the adsorption site locations. Additionally, two initial configurations for the CO molecule, vertical and horizontal (see Figure S20), were considered to comprehensively explore favorable adsorption configurations. For CO adsorption simulations, the C atom was positioned 2 Å above an O atom near a Si or Ni atom to ensure appropriate bonding and charge matching between the positively charged C atom and the negatively charged O atom. To mitigate dipole effects in the surface model, CO molecules were symmetrically adsorbed on both sides of the slab.

DFT Calculation Details

DFT calculations were conducted using the Vienna *ab initio* simulation package (VASP)[6] with the Perdew–Burke–Ernzerhof (PBE) generalized gradient approximation (GGA).[7] The projector-augmented wave (PAW)[8] method was applied in all calculations, and van der Waals

interactions[9] were accounted for using the DFT-D3 dispersion correction method. The valence electron configurations considered were $3d^{10}4s^1$ for Cu and $3d^9 4s^1$ for Ni. For bulk structures, both atomic positions and lattice parameters were optimized to minimize internal stress. In the case of surface structures (slab model), only the atomic positions were allowed to relax. Geometry optimization was performed with a cutoff energy of 500 eV, and partial orbital occupancies were described using Gaussian smearing with a width of 0.03 eV. The convergence criteria for electronic and ionic relaxation were set to energy differences of 10^{-5} eV and forces less than 0.03 eV/Å, respectively. The first Brillouin zone was sampled using a Monkhorst–Pack mesh with a 3 × 3 × 1 k-point grid.

The adsorption energy (E_{ad}) was calculated using the following equation:

$$E_{ad} = \frac{(E_{final} - E_{support} - 2E_{adsorbate})}{2}$$

where E_{final} is the total energy of the adsorbed structure (CO on the Ni or Cu surface), E_{support} is the energy of the substrate, calculated to be -1015.59 eV for Ni (with 176 atoms) and -596.21 eV for Cu (with 144 atoms), and $E_{\text{adsorbate}}$ is the energy of the adsorbate, one CO molecule, calculated to be -14.79 eV in an isolated cell. The factor of two in front of $E_{\text{adsorbate}}$ and the division by two account for adsorption of CO on both sides of the surface.

Charge Density Difference Analysis

Charge density difference analysis was conducted to evaluate the charge transfer induced by CO adsorption on the Ni and Cu surfaces. This was done by subtracting the charge density distributions of the isolated CO molecule and the clean metal surface from the charge density distribution of the CO-adsorbed metal surface. This approach highlights the redistribution of electron density due to the adsorption process.

Table S1. Metal content, H_2 uptake, EOR and porosity of exsolved and impregnated catalysts

Catalyst	Metal content (wt%)[a]	D (%)[b]	H_2 uptake (mmol g_{Me}^{-1})	EOR (%)[c]	LAS (µmol g^{-1})[d]	S_{BET} (m^2 g^{-1})	S_{micro} (m^2 g^{-1})	V_{total} (cm^3 g^{-1})	V_{micro} (cm^3 g^{-1})
Cu@S-1-red	2.8	23.3	8.3	66.0	25.2	337	219	0.19	0.10
Ni@S-1-red	3.8	1.6	8.2	61.2	17.5	341	292	0.18	0.13
Cu/S-1-red	1.8	23.3	9.5	75.5	9.8	457	264	0.46	0.12
Ni/S-1-red	2.7	1.6	8.6	64.5	3.5	454	280	0.46	0.12

[a]Calculated from ICP-OES

[b]Estimated using Scherrer equation[10]

[c]Calculated as mole of consumed H_2 / mole of H_2 needed to reduce Ni^{2+} or Cu^{2+} to Ni^0 or Cu^0 respectively

[d]Calculated using Py-IR adsorption

Table S2. Parameters obtained from the fitting results of the EXAFS data at Cu and Ni *K*-edges of the tested catalysts.

Sample	Scattering path	CN[a]	R (Å)[b]	σ^2 (Å^2)[c]	R-factor
Cu@S-1-red	1st (Cu-O)	2.6 ± 0.5	1.92	0.004	0.04
	2nd (Cu-Cu)	0.4 ± 0.3	2.57	0.001	
Ni@S-1-red	1st (Ni-O)	0.6 ± 1.5	2.01	0.001	0.01
	2nd (Ni-Ni)	9.7 ± 3.1	2.49	0.007	
Cu/S-1-red	1st (Cu-O)	2.3 ± 1.3	1.92	0.004	0.10
	2nd (Cu-Cu)	1.3 ± 1.8	2.57	0.002	
Ni/S-1-red	1st (Ni-O)	1.3 ± 2.4	2.01	0.002	0.01
	2nd (Ni-Ni)	10.3 ± 4.2	2.49	0.008	

a: coordination number; b: interatomic distance; c: Debye-Waller factor

Table S3. RWGS performance of various catalysts reported in literature

Catalyst	Synthesis method	Reaction condition	X_{CO2} (%)	S_{CO} (%)	Ref.
Cu@S-1-red	Exsolution	T=400 °C, CO_2/H_2 = 1/3, GHSV= 6000 mL g_{cat}^{-1} h^{-1}	31.0	100	This work
Ni@S-1-red			32.8	84.7	
Cu/S-1-red	Incipient wetness impregnation		6.1	100	
Ni/S-1-red			37.7	9.0	
Cu/SiO_2			5.3	100	
Ni/SiO_2			14.7	61.3	
Ni/Ga_2O_3	Incipient wetness impregnation	T= 450 °C, CO_2/H_2 = 1/4	37.9	97.4	11
1Cu/CeO_2	Solution combustion synthesis	T= 600 °C, CO_2/H_2 = 1/4, flowrate = 50 sccm	70	100	12
NiCo@SiO_2	Hard template method	T= 400 °C, CO_2/H_2 = 1/4, WHSV= 15 L/g_{cat} h	40	42	13
1Ni-2Ga/Al_2O_3	Incipient wetness impregnation	T= 400 °C, CO_2/H_2 = 1/4, WHSV= 30,000 mL g_{cat}^{-1} h^{-1}	10	23	14
Ni-0.3Ag/SiO_2	Incipient wetness co-impregnation	T= 400 °C, CO_2/H_2 = 1/4, GHSV= 100 L g^{-1} h^{-1}	10.7	93.2	15
2Ni@PS	Urea-assisted ammonia evaporation hydrothermal	T= 450 °C, CO_2/H_2= 1/3, GHSV= 6000 mL g_{cat}^{-1} h^{-1}	40	51	1
0.2Ni/S-1	Incipient wetness impregnation		55	38.3	
0.2Ni@S-1	Hydrothermal		40	99.9	
Cu-hydrotalcite	Co-precipitation	T= 400 °C, CO_2/H_2 = ¼, flowrate= 100 mL min^{-1}	38	35	16
10Cu-1Fe/MCM-41	Hydrothermal	T= 400 °C, CO_2/H_2 = 1/3, WHSV= 96,000 mL g^{-1} h^{-1}	18	33	17

Table S4. The DFT-calculated lattice parameters of Ni and Cu metal bulk structures, both are cubic phases ($Fm\bar{3}m$)

		***a* (Å)**
Ni bulk	Initial Structure[18]	3.500
	DFT-optimized Structure	3.517
	Experiment[19]	3.524
	Deviation	0.20%
Cu bulk	Initial Structure[20]	3.577
	DFT-optimized Structure	3.631
	Experiment[19]	3.615
	Deviation	0.44%

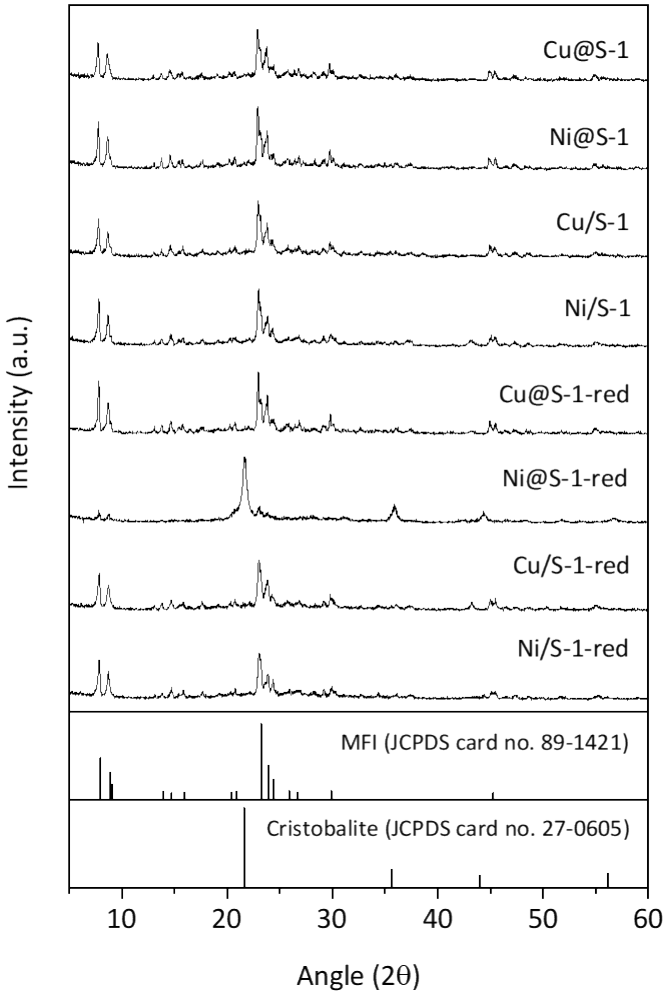

Figure S1. XRD patterns of unreduced precursors and reduced catalysts

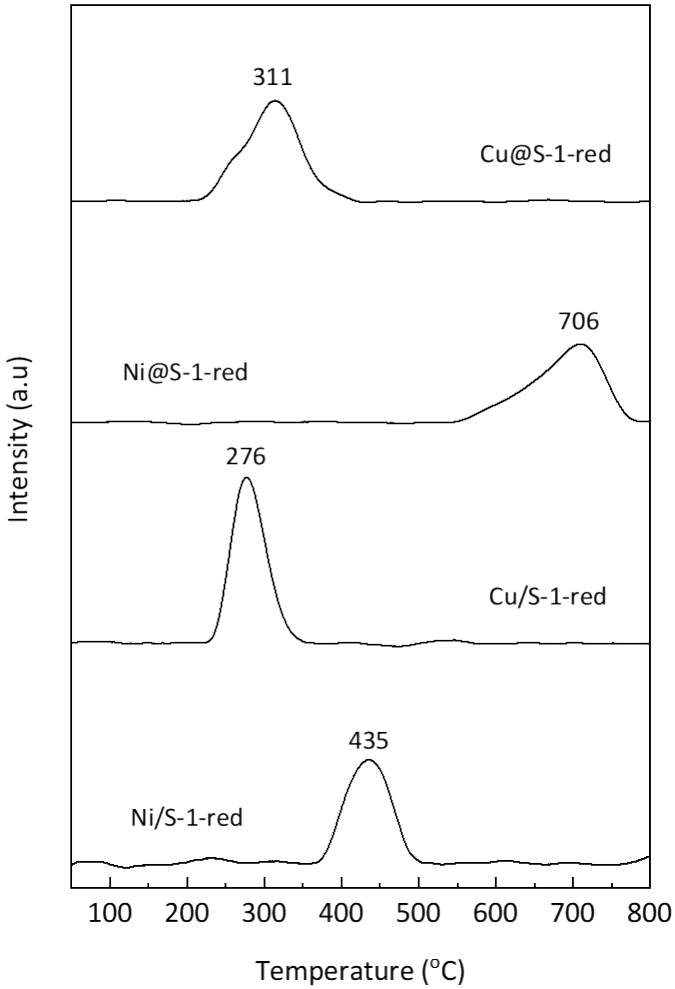

Figure S2. H_2-TPR profile of the exsolved and impregnated catalysts

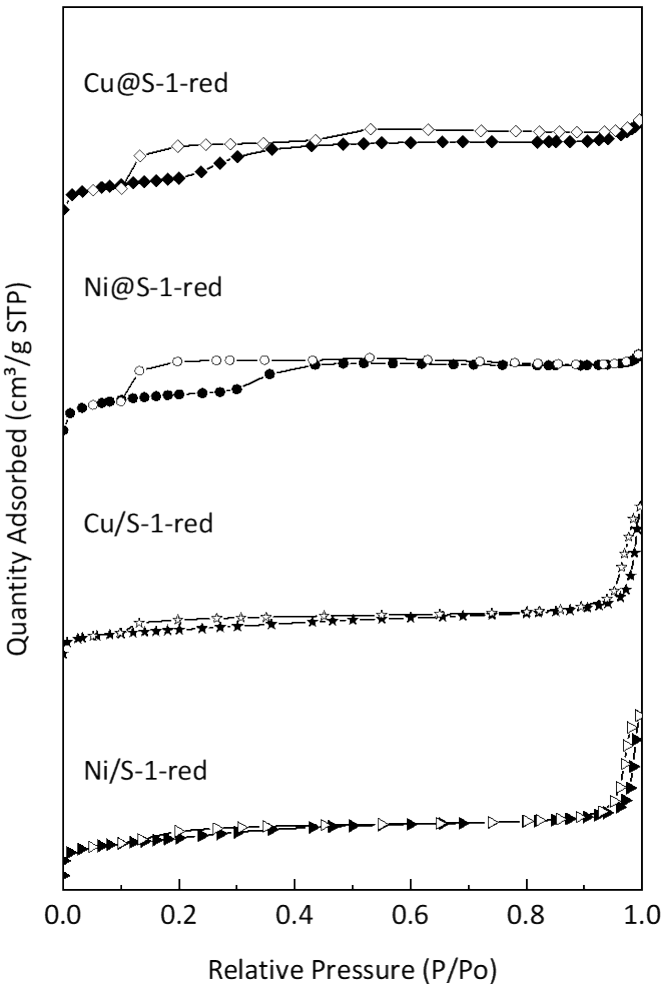

Figure S3. N_2 isotherms of the exsolved and impregnated catalysts

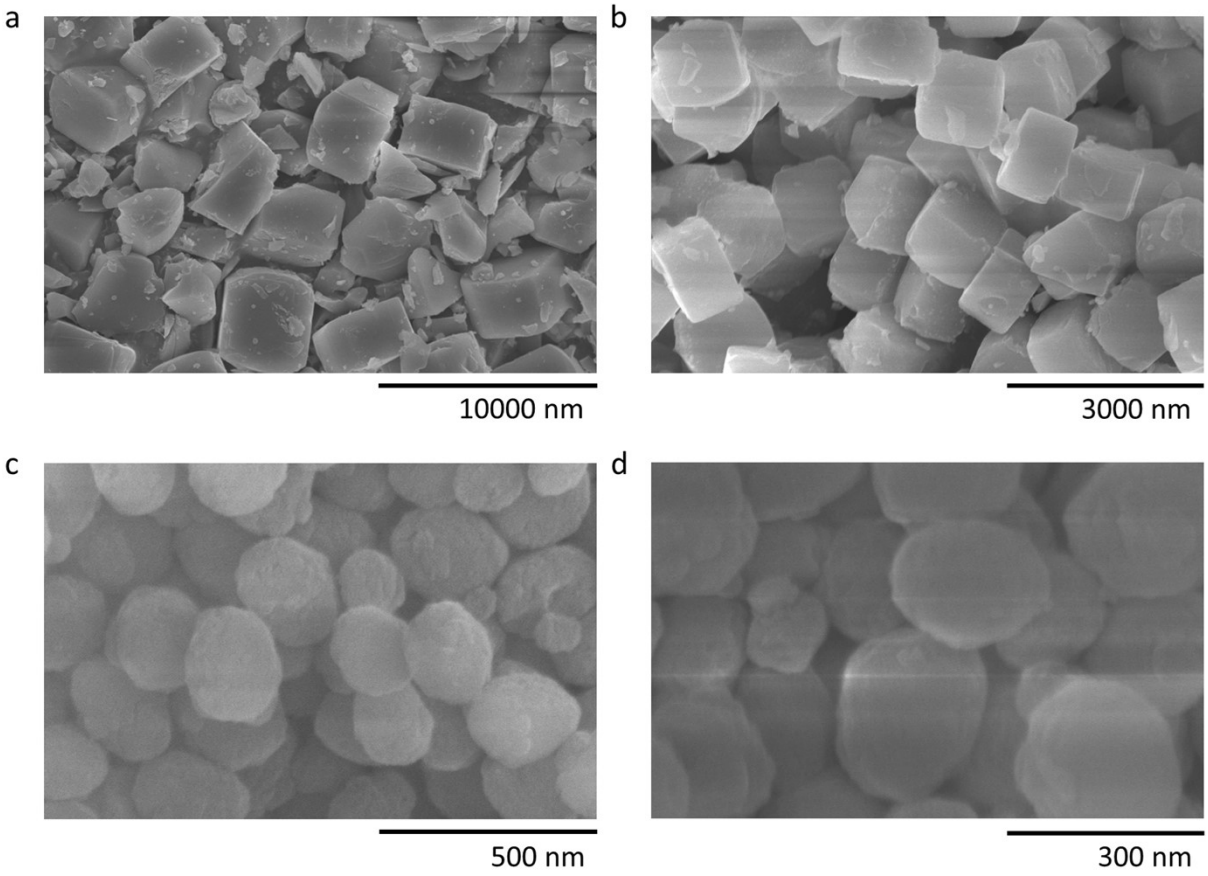

Figure S4. SEM images of (a) Cu@S-1-red, (b) Ni@S-1-red, (c) Cu/S-1-red, and (d) Ni/S-1-red

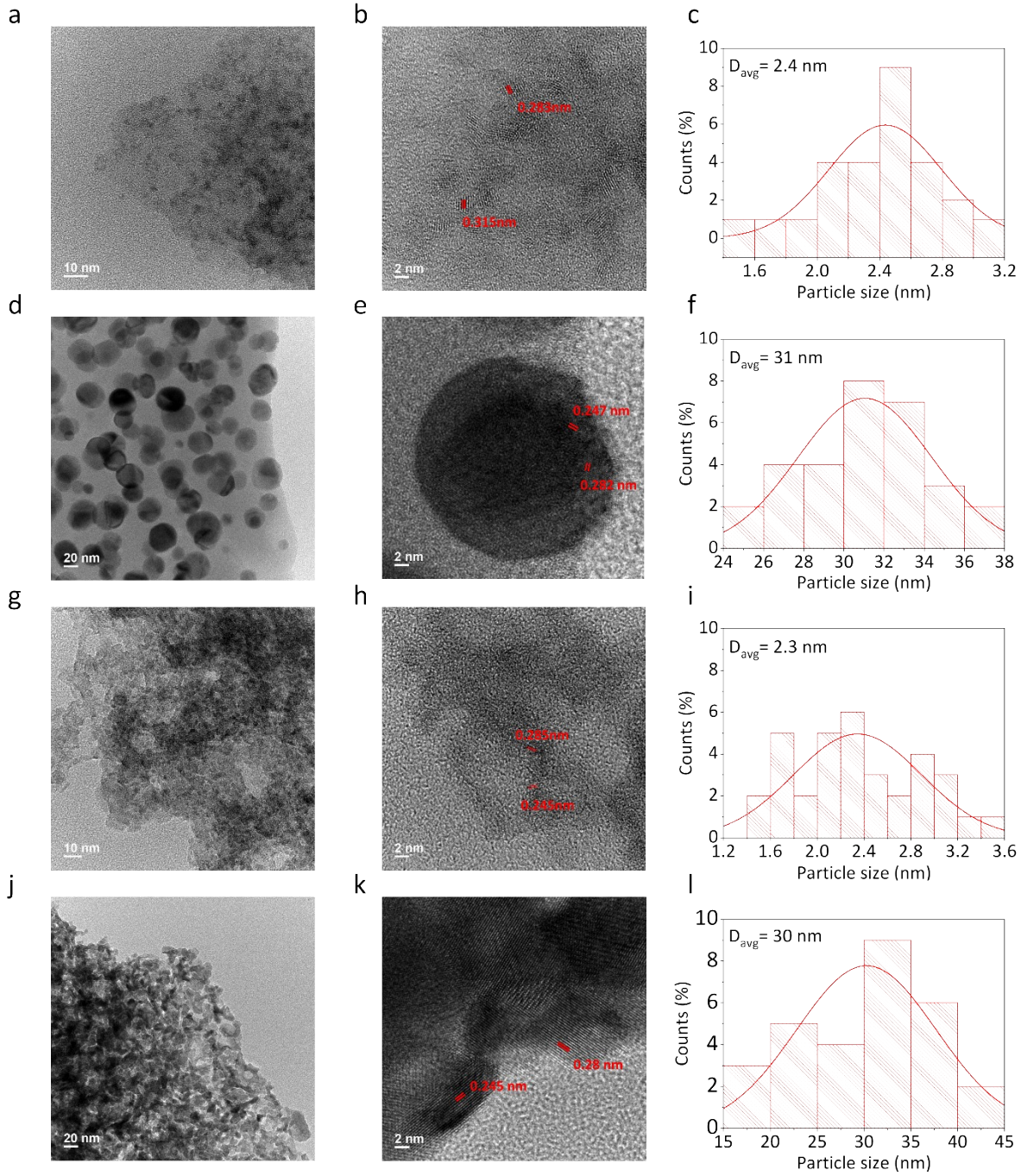

Figure S5. HR-TEM images and particle size distribution of (a-c) Cu@S-1-red, (d-f) Ni@S-1-red, (g-i) Cu/S-1-red, and (j-l) Ni/S-1-red

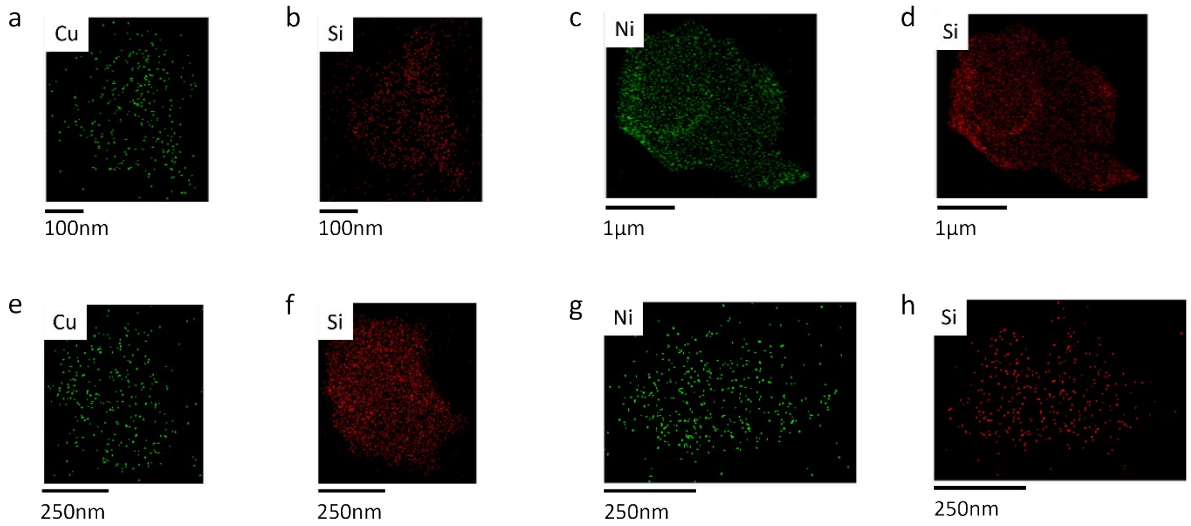

Figure S6. EDS mapping of (a, b) Cu@S-1-red, (c, d) Ni@S-1-red, (e, f) Cu/S-1-red, and (g, h) Ni/S-1-red

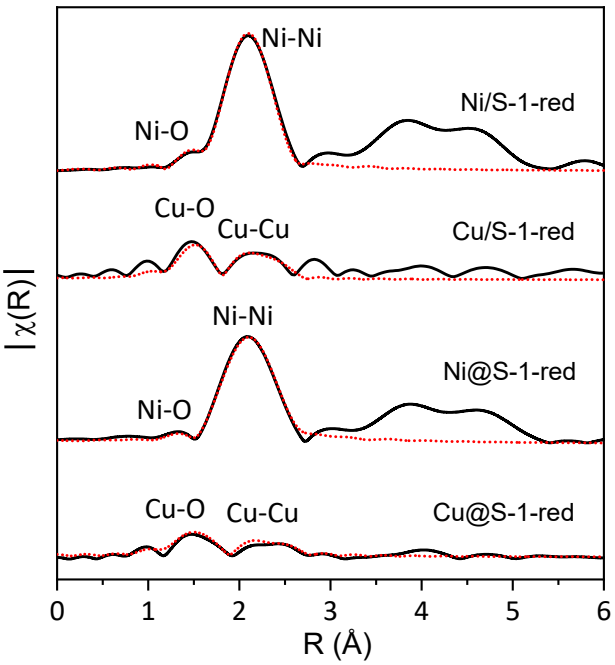

Figure S7. XAS fitting curves in R-space (uncorrected for the phase shift) of the tested catalysts

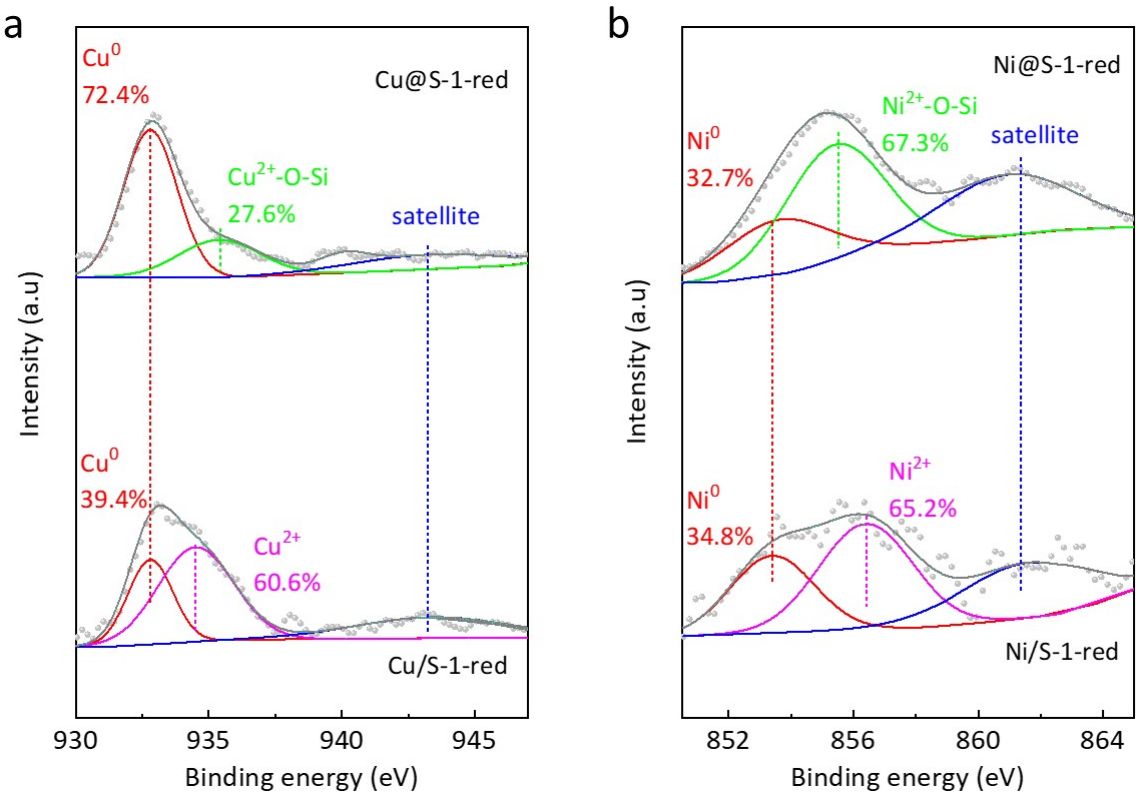

Figure S8. XPS spectra of (a) Cu@S-1-red and Cu/S-1-red and (b) Ni@S-1-red and Ni/S-1-red catalysts. The $Cu_{2p3/2}$ peak could be deconvoluted into Cu^0 (932.8 eV), Cu^{2+}-O-Si (935.4 eV), Cu^{2+} (934.5 eV), and satellite peak (943.2 eV).[21-23] Meanwhile, the $Ni_{2p3/2}$ could be deconvoluted into Ni^0 (853.4 eV), Ni^{2+}-O-Si (855.5 eV), Ni^{2+} (856.4 eV), and satellite peak (861.3 eV).[1, 24, 25]

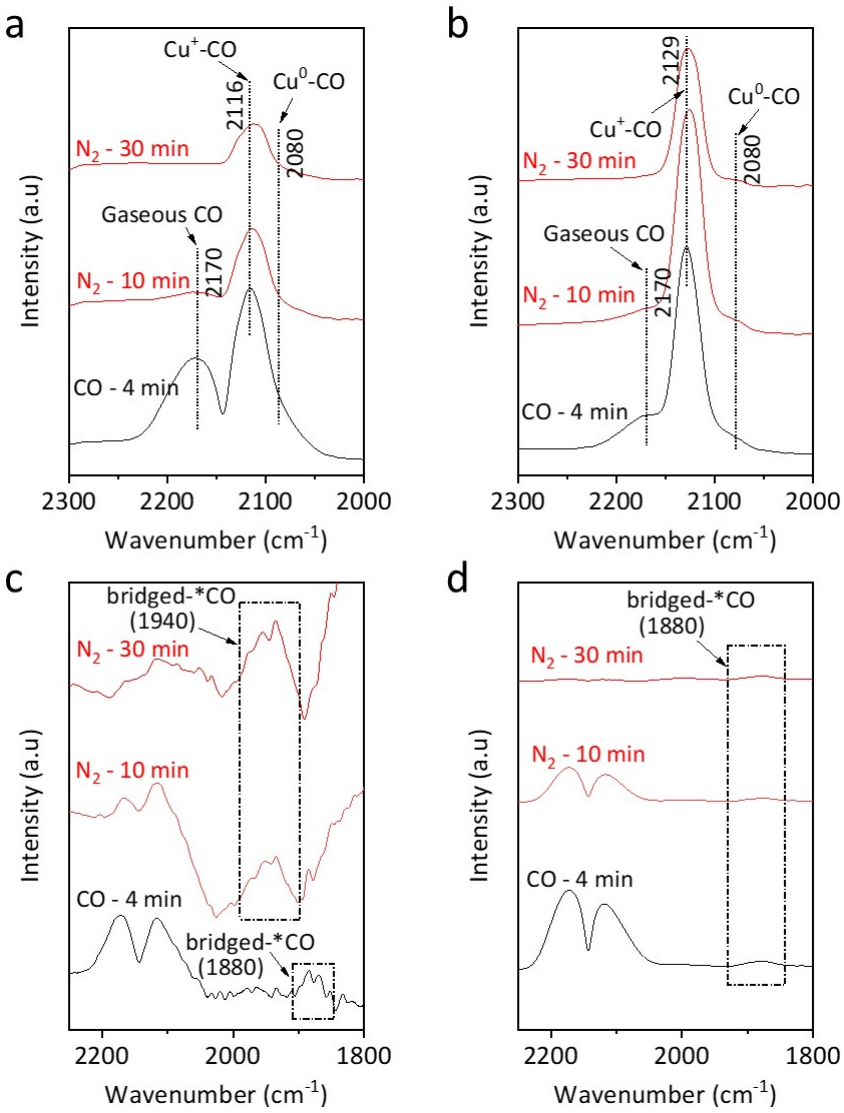

Figure S9. DRIFTS spectra of CO adsorption at 50 °C followed by N_2 flushing of (a) Cu@S-1-red, (b) Cu/S-1-red, (c) Ni@S-1-red, and (d) Ni/S-1-red

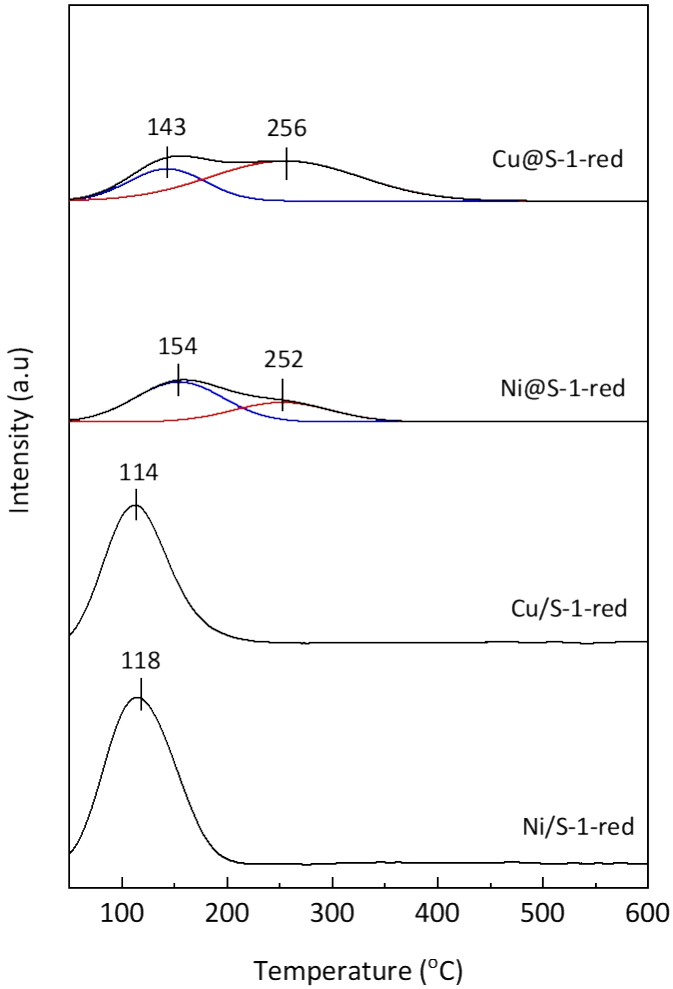

Figure S10. NH_3-TPD of exsolved and impregnated catalysts

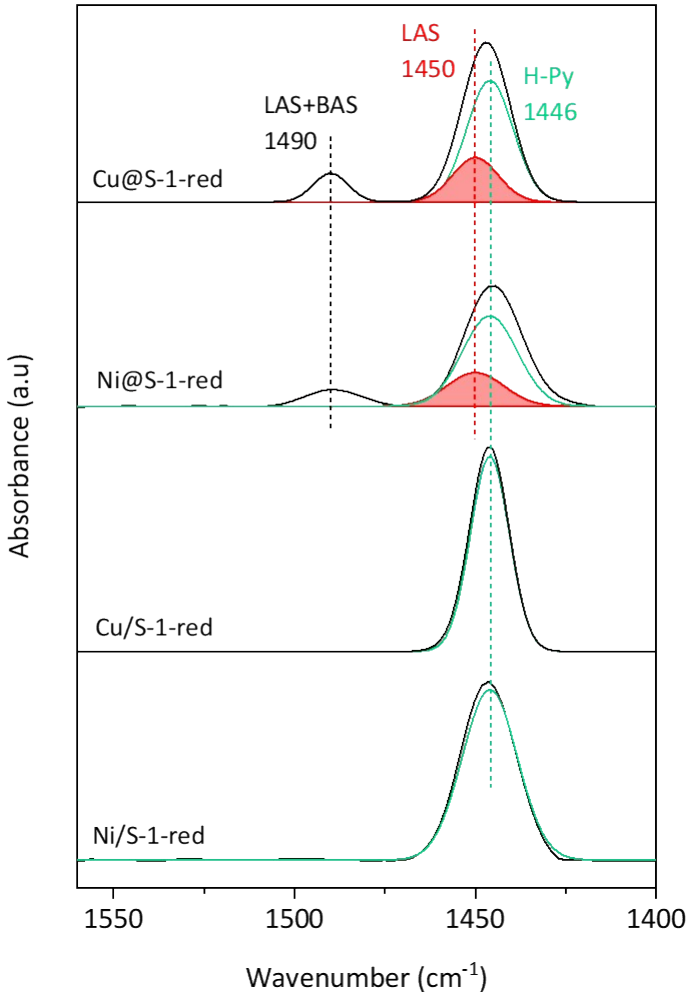

Figure S11. Py-IR spectra at 150 °C of exsolved and impregnated catalysts. The peaks assigned to H-Py (1446 cm^{-1}), LAS (1450 cm^{-1}), and LAS+BAS (1490 cm^{-1}) followed the reference.[1]

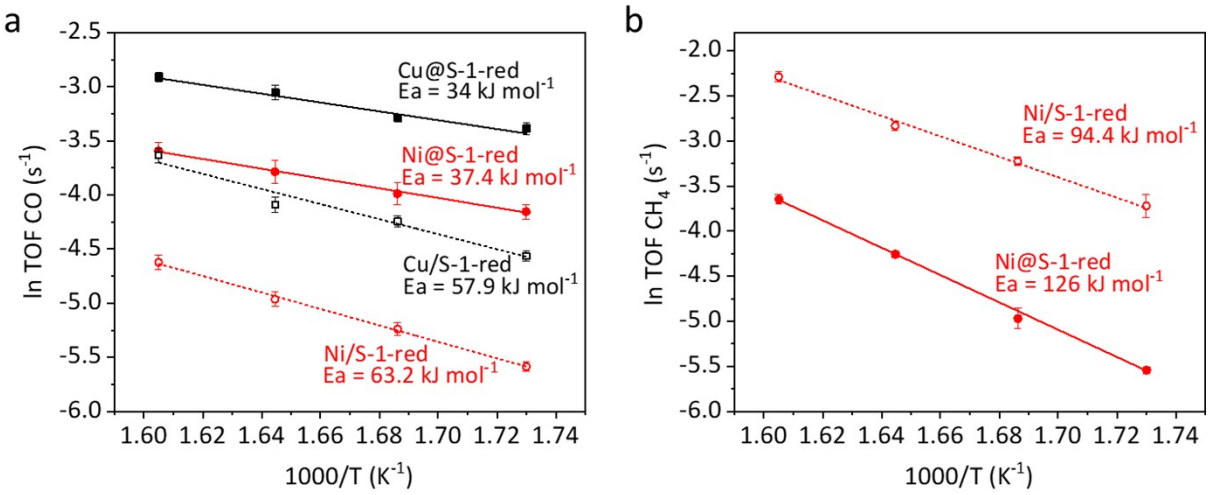

Figure S12. Arrhenius plots for the TOFs of (a) CO and (b) CH_4 of exsolved and impregnated catalysts (GHSV = 72000 mL g_{cat} h^{-1}, CO_2/H_2 = 1/1)

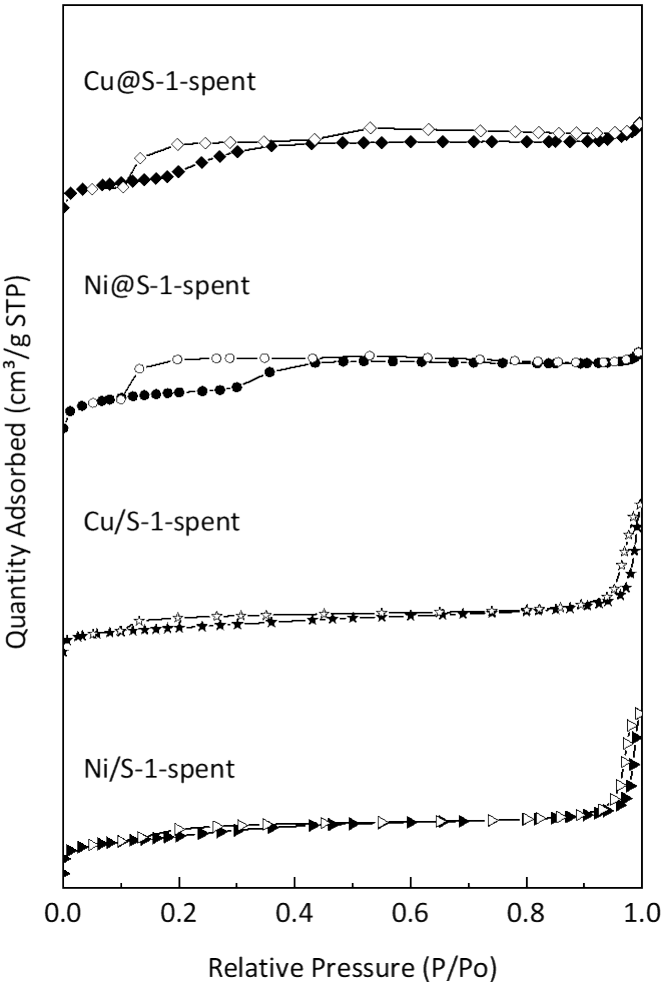

Figure S13. N_2 isotherms of the spent exsolved and impregnated catalysts

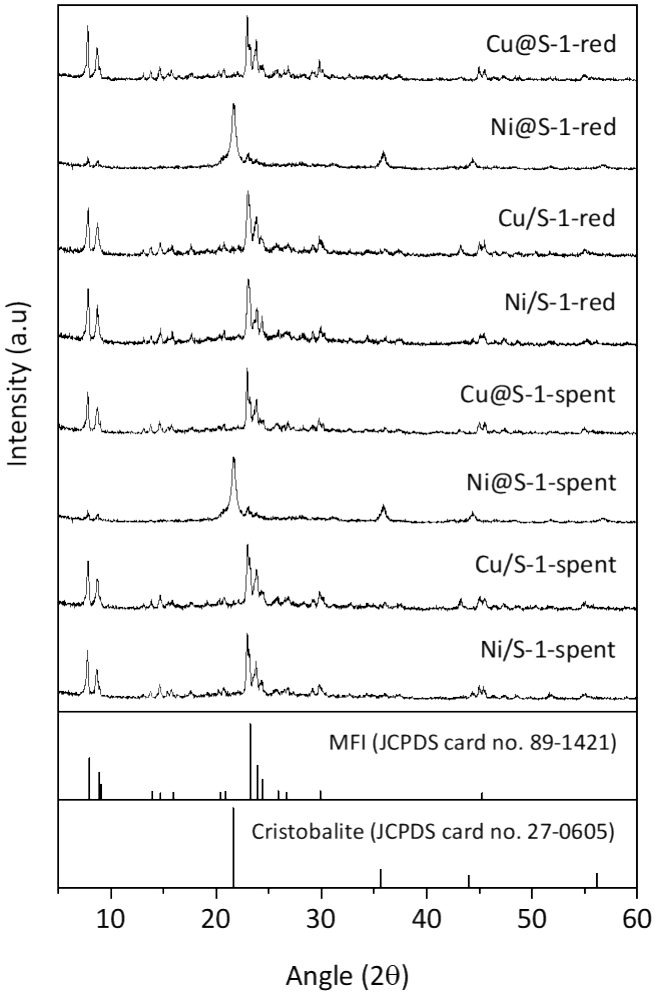

Figure S14. XRD patterns of the fresh and post-reaction catalysts

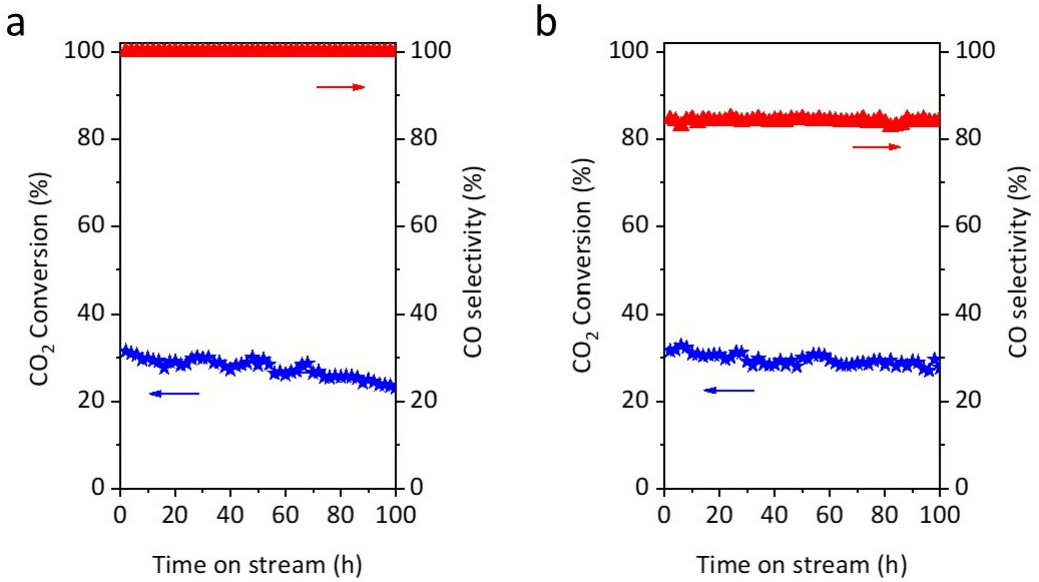

Figure S15. 100 h on-stream test of (a) Cu@S-1-red and (b) Ni@S-1-red. Reaction conditions: T= 400 °C, GHSV = 6000 mL g_{cat} h^{-1}, $CO_2/H_2/N_2$ = 12.5/37.5/50, 0.2 g catalyst, 1 bar.

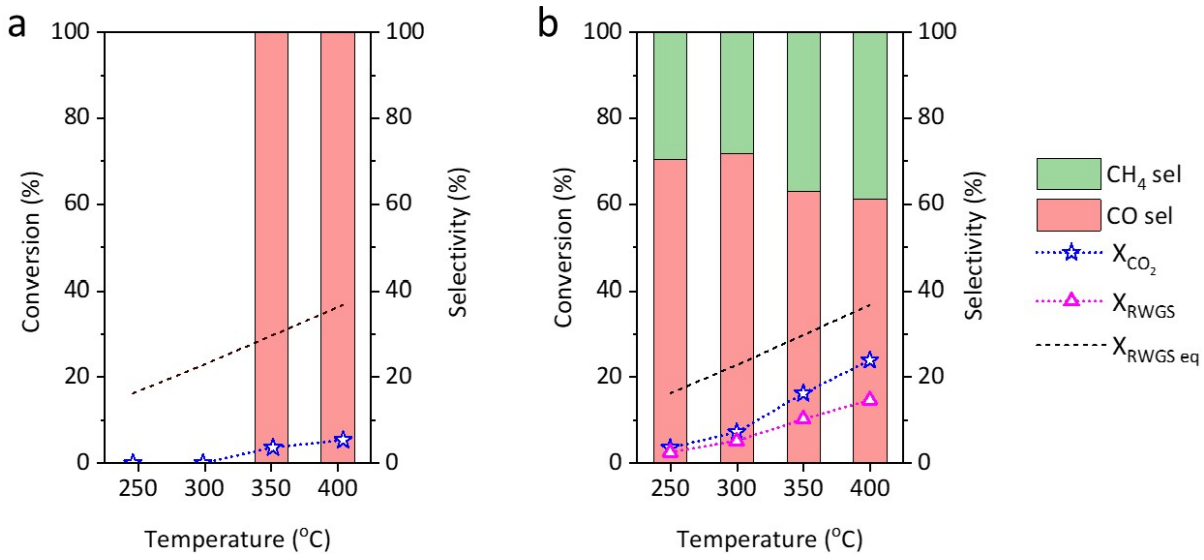

Figure S16. RWGS activity of (a) Cu/SiO_2 and (b) Ni/SiO_2. Reaction conditions: GHSV = 6000 mL g_{cat} h^{-1}, $CO_2/H_2/N_2$ = 12.5/37.5/50, 0.2 g catalyst, 1 bar.

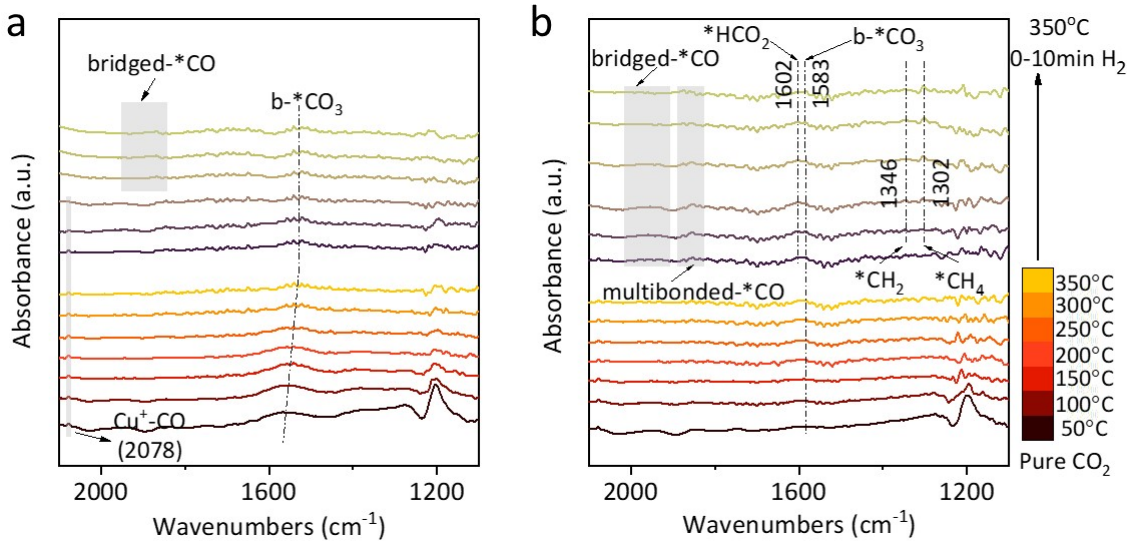

Figure S17. In-situ DRIFTS spectra of CO_2-H_2 switching test of (a) Cu/S-1-red and (b) Ni/S-1-red

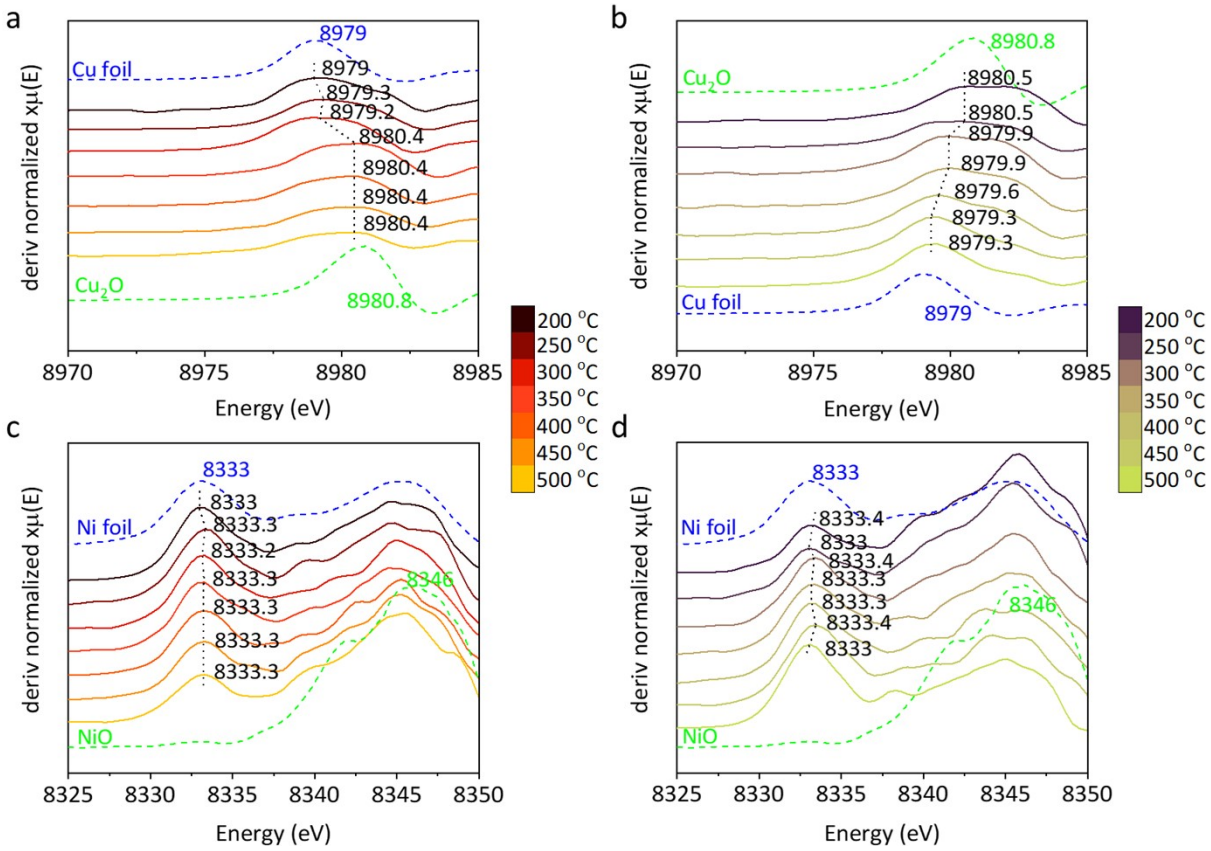

Figure S18. Edge shifts of Cu@S-1-red under (a) CO_2 and (b) H_2 environments, and Ni@S-1-red under (c) CO_2 and (d) H_2 environments. Cu and Ni references were taken from Ji et al.[26] and Chen et al.[1]

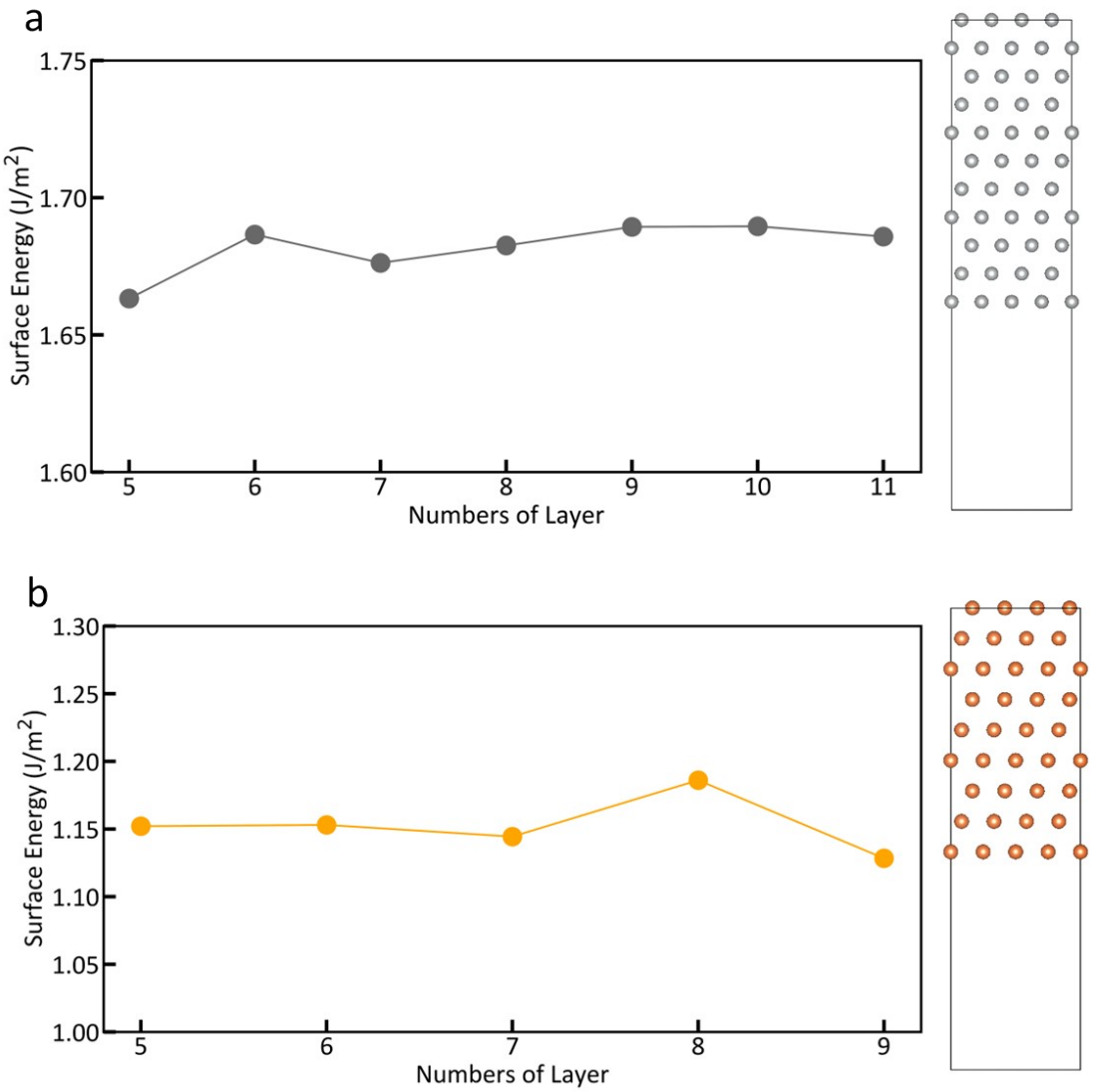

Figure S19. Convergence test of surface energy with varying numbers of layers for the (111) surfaces of (a) Ni and (b) Cu metals, along with the final surface atomic structures used for subsequent CO adsorption analysis

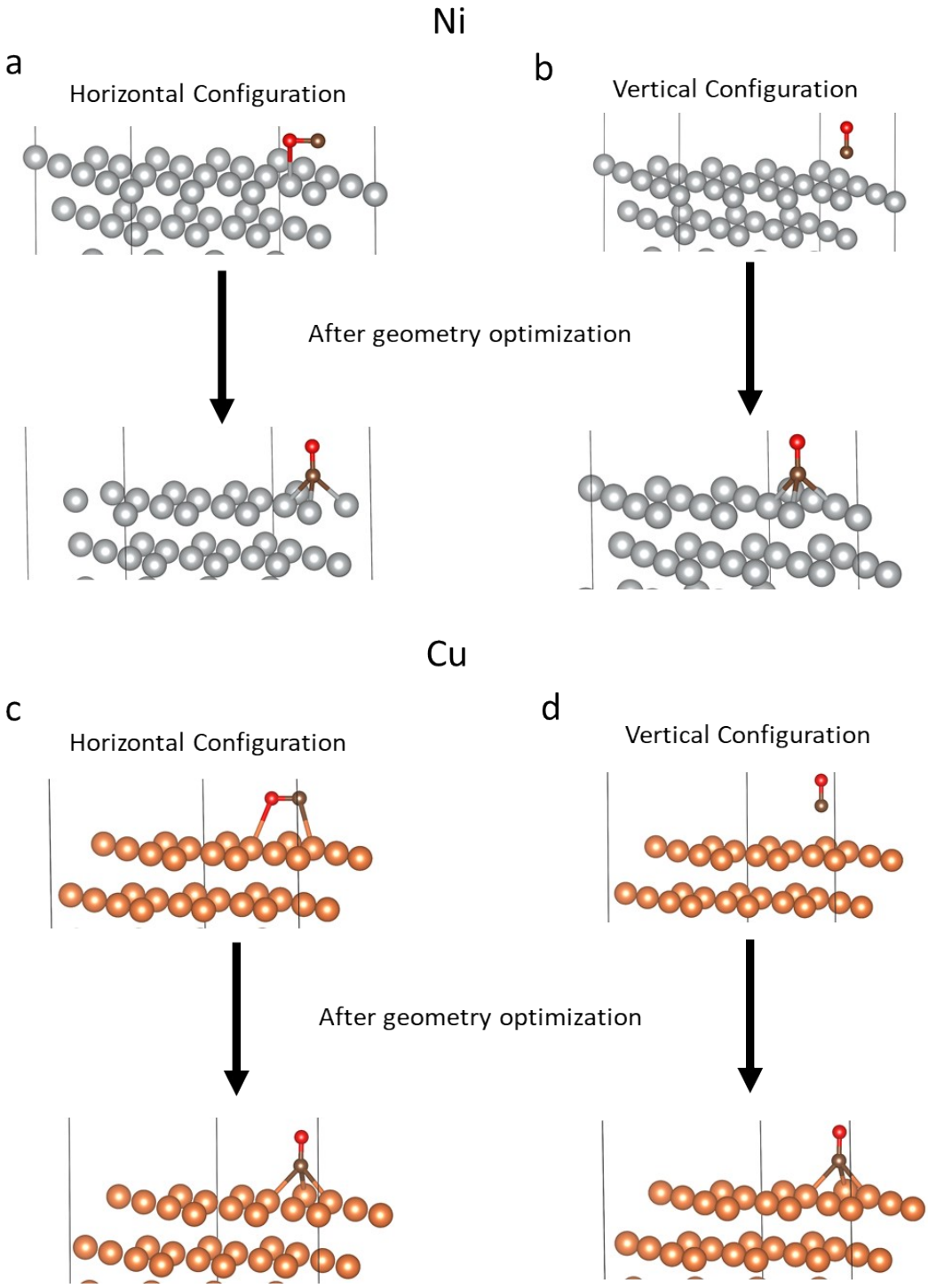

Figure S20. Two initial configurations of the CO molecule—horizontal and vertical—on the (111) surfaces of (a-b) Ni and (c-d) Cu, used for DFT optimization. The corresponding geometry-optimized structures are also shown

References

1. C.-H. Chen, H.-K. Chen, W.-H. Huang, C.-L. Chen, K. Choojun, T. Sooknoi, H.-K. Tian and Y.-C. Lin, *Green Chem.*, 2023, **25**, 7582-7597.
2. R. Bodlos, V. Fotopoulos, J. Spitaler, A. L. Shluger and L. Romaner, *Materialia*, 2022, **21**, 101362.
3. Z. Ou, C. Qin, J. Niu, L. Zhang and J. Ran, *Int. J. Hydrogen Energy*, 2019, **44**, 819-834.
4. J. Y. Lee, M. P. J. Punkkinen, S. Schönecker, Z. Nabi, K. Kádas, V. Zólyomi, Y. M. Koo, Q. M. Hu, R. Ahuja, B. Johansson, J. Kollár, L. Vitos and S. K. Kwon, *Surf. Sci.*, 2018, **674**, 51-68.
5. S. P. Ong, W. D. Richards, A. Jain, G. Hautier, M. Kocher, S. Cholia, D. Gunter, V. L. Chevrier, K. A. Persson and G. Ceder, *Comput. Mater. Sci.*, 2013, **68**, 314-319.
6. G. Kresse and J. Furthmüller, *Phys. Rev. B*, 1996, **54**, 11169-11186.
7. J. P. Perdew, K. Burke and M. Ernzerhof, *Phys. Rev. Lett.*, 1996, **77**, 3865-3868.
8. G. Kresse and D. Joubert, *Phys. Rev. B*, 1999, **59**, 1758-1775.
9. S. Grimme, *J. Comput. Chem.*, 2006, **27**, 1787-1799.
10. A. Borodziński and M. Bonarowska, *Langmuir*, 1997, **13**, 5613-5620.
11. J. Gong, M. Chu, W. Guan, Y. Liu, Q. Zhong, M. Cao and Y. Xu, *Ind. Eng. Chem. Res.*, 2021, **60**, 9448-9455.
12. P. Ebrahimi, A. Kumar and M. Khraisheh, *Int. J. Hydrogen Energy*, 2022, **47**, 41259-41267.
13. C. A. H. Price, L. Pastor-Perez, T. R. Reina and J. Liu, *Catal. Today*, 2022, **383**, 358-367.
14. A. M. Bahmanpour, R. J. G. Nuguid, L. M. Savereide, M. D. Mensi, D. Ferri, J. S. Luterbacher and O. Kröcher, *J. CO2 Util.*, 2022, **57**, 101881.
15. C. Zhang, R. Zhang, Y. Liu, X. Wu, H. Wang, Q. Ge and X. Zhu, *ChemCatChem*, 2023, **15**, e202201284.
16. D. Álvarez-Hernández, M. Marín-Sánchez, L. Lobo-Andrades, L. Azancot, L. F. Bobadilla, S. Ivanova and M. A. Centeno, *Catal. Today*, 2023, **422**, 114235.
17. M. R. Kiani, R. Kamandi, K. Nozarian and M. R. Rahimpour, *Energy Convers. Manage.*, 2024, **304**, 118247.
18. W. P. Davey, *Phys. Rev.*, 1925, **25**, 753-761.
19. V. A. Lubarda, *Mech. Mater.*, 2003, **35**, 53-68.
20. S. H. Wei, A. A. Mbaye, L. G. Ferreira and A. Zunger, *Phys. Rev. B*, 1987, **36**, 4163-4185.
21. S. Bawaked and K. Narasimharao, *Sci. Rep.*, 2020, **10**, 518.
22. P. Cornette, S. Zanna, A. Seyeux, D. Costa and P. Marcus, *Corros. Sci.*, 2020, **174**, 108837.
23. W. Feng, Z. Xiao, B. Chen, Y. Pi, C. Hu, W. Zhang, Q. Meng and T. Wang, *Int. J. Hydrogen Energy*, 2024, **61**, 113-124.
24. I. Czekaj, F. Loviat, F. Raimondi, J. Wambach, S. Biollaz and A. Wokaun, *Appl. Catal., A*, 2007, **329**, 68-78.
25. T. Pu, L. Shen, X. Liu, X. Cao, J. Xu, I. E. Wachs and M. Zhu, *J. Catal.*, 2021, **400**, 228-233.
26. Y. Ji, Z. Chen, R. Wei, C. Yang, Y. Wang, J. Xu, H. Zhang, A. Guan, J. Chen, T.-K. Sham, J. Luo, Y. Yang, X. Xu and G. Zheng, *Nat. Catal.*, 2022, **5**, 251-258.